Available online at www.sciencedirect.com
ScienceDirect
Ceramics International 36 (2010) 1429–1437
CERAMICS INTERNATIONAL
www.elsevier.com/locate/ceramint

Kinetic field approach to study liquid phase sintering of ZnO based ceramics

Friedrich Raether *, Mohammad Lutful Arefin

Fraunhofer-Institut Silicatforschung (ISC), Neunerplatz 2, 97082 Würzburg, Germany

Received 28 December 2009; received in revised form 10 January 2010; accepted 2 February 2010
Available online 1 March 2010

Abstract

Liquid phase sintering kinetics in the system ZnO–Bi_2O_3–Sb_2O_3 was studied using closed crucibles and an optical dilatometer. A modified kinetic field technique was applied for the first time to investigate the densification rates. The values obtained were assessed with existing liquid phase sintering models. Grain growth data were derived from the kinetic field diagram and compared to those obtained from microstructure analysis of quenched samples. Good agreement was obtained between both techniques. Values for both the activation energies (activation energies for grain growth and densification) were also reported for the ZnO–Bi_2O_3–Sb_2O_3 system for the first time. In the initial sintering stage mechanisms were identified which retard densification and are essentially unaffected by temperature. It was shown how the position and slope of the iso-strain lines in the modified kinetic field diagram can be used for a qualitative understanding of the interaction of coarsening, liquid redistribution and densification during sintering.

Keywords: E. Varistors; Liquid phase sintering; Optical dilatometer; Kinetic field analysis

1. Introduction

Since the early seventies, when it was first reported by Matsuoka [1], ZnO has become the most popular industrial ceramic for metal oxide varistor (MOV) fabrication. The varistor functionality results from the semiconductive ZnO grains, separated by a dielectric grain boundary layer [2]. It has been agreed that varistor functionality in MOVs generally result from Schottkey barriers formed at the grain boundaries [3,4]. The most important component for varistor activity across the ZnO-grain boundaries is bismuth oxide which creates a thin layer in the nano to micron range around ZnO grains.

The voltage at the grain boundary where the switching from linear current–voltage characteristic to break down takes place is approximately 3.0–3.6 V—almost independent of the composition of the varistor [5,6]. Therefore, the macroscopic break down voltage of a varistor depends on the number of grain boundaries, i.e. its grain size and its length. A homogenous grain size distribution is aimed at to avoid break down along any favoured current paths which reduces the lifetime of varistors [7]. A zinc-antimonate spinel ($Zn_7Sb_2O_{12}$) [8,9] is typically used to reduce grain growth in ZnO based varistor ceramics [2]. The spinel is formed from antimony oxides added as sintering aid. The grain growth controlling mechanism was related to the Zener drag process involving spinel particles located at the ZnO grain boundaries [2].

The ternary system ZnO–Bi_2O_3–Sb_2O_3 shows a number of microstructural and phase changes during sintering. Bi_2O_3 forms a liquid by eutectic melting with ZnO at 738 °C [10], which enables liquid phase sintering. Sb_2O_3, Bi_2O_3 and ZnO form a pyrochlore phase at temperatures between 500 and 700 °C [8]. The pyrochlore phase decomposes at higher temperatures (>1000 °C) to form the spinel and additional melt phase [11].

The most important densification mechanisms during liquid phase sintering are contact flattening and Ostwald ripening. Both mechanisms are active during solution and reprecipitation in the intermediate sintering stage. They are described by equations of identical structure [12,13]:

$$-\frac{\Delta L}{L_0} = \left(\frac{CD_l\gamma_l}{G^n T}\right)^{1/3} t^{1/3}; \qquad D = D_0 \exp\left(-\frac{E_D}{RT}\right);$$
$$G^m = G_0^m + k_0 \exp\left(-\frac{E_G}{RT}\right) t; \tag{1}$$

where $\Delta L/L_0$ = sintering shrinkage, C = constant depending on sintering state, D_l = diffusion coefficient of atoms of solid

* Corresponding author. Tel.: +49 0931 4100 200; fax: +49 0931 4100 299.
E-mail address: friedrich.raether@isc.fraunhofer.de (F. Raether).

0272-8842/$36.00
doi:10.1016/j.ceramint.2010.02.002

Table 1
Exponents m and activation energies E_G for ZnO grain growth in various ZnO based ceramic systems.

Reference	Ceramic system	Grain-growth exponent, m	E_G (kJ/mol)
Senda and Bradt [14]	ZnO	3	224 ± 16
Senda and Bradt [14]	ZnO–Bi_2O_3	5	150
Dey and Bradt [15]	ZnO–Bi_2O_3	5	178–274
Senda and Bradt [16]	ZnO–Sb_2O_3	6	600
Nunes [17]	ZnO–Bi_2O_3–Al_2O_3	4	400
Suzuki and Bradt [18]	ZnO–Bi_2O_3–TiO_2	3	360
Chen et al. [19]	ZnO–Bi_2O_3–Sb_2O_3–Cr_2O_3–CoO–MnO	6	301 ± 35

phase within the melt phase, γ_{lv} = energy of liquid–vapour interface, G = grain size, G_0 = initial grain size, D_0 and k_0 are constant frequency factors, R = gas constant, E_D and E_G are the activation energies for diffusion respectively grain growth, T = absolute temperature, t = time, n = scaling exponent depending on rate controlling mechanism ($n = 3$ for Ostwald ripening and $n = 4$ for contact flattening) and m = grain growth exponent ($m = 3$ for diffusion controlled Ostwald ripening).

Attempts were made to elucidate the contribution of additive oxides on the grain growth controlling mechanisms of ZnO (Table 1). Two groups [14,15] investigated the effect of Bi_2O_3-content on the grain growth of ZnO, using 1–4 wt% [14] and 3–12 wt% [15] Bi_2O_3. For the 1–4 wt% range, the grain size of ZnO increased at initial additions, but then it remained constant and showed a fairly consistent activation energy of 150 kJ/mol. For the 3–12 wt% range, activation energy was in a range of 178–274 kJ/mol and ZnO-grain growth was found to decrease with increasing Bi_2O_3 content. Spinel forming additives were studied by Senda and Bradt [16] who reported a significant reduction of ZnO grain sizes and activation energy for grain growth of 600 kJ/mol. Two works involved ternary systems, taking Al_2O_3 [17] and TiO_2 [18] as a third additive in the binary ZnO–Bi_2O_3 system. Al_2O_3 and TiO_2 formed a $ZnAl_2O_4$ spinel and a Zn_2TiO_4 spinel, respectively. The activation energies for grain growth were 400 kJ/mol for the alumina containing system and 360 kJ/mol for the titania containing system. Chen et al. [19] studied the multi-component varistor system: ZnO, Sb_2O_3, Bi_2O_3, Cr_2O_3, CoO and MnO. In their work, the grain growth exponent m was 6 and the activation energy was 301 ± 35 kJ/mol.

In the present study the kinetic field method and optical dilatometry will be applied to study densification and grain growth in the ZnO–Bi_2O_3–Sb_2O_3 system. Although this ternary system is a simplified model for real varistor ceramics, which requires about 10 different additives [3], it is considered to be sufficient to learn about the optimisation of process conditions in rather complex liquid phase sintered ceramics.

2. Experimental techniques

2.1. Sample preparation

ZnO–Sb_2O_3–Bi_2O_3 (ZBS) green samples were prepared after dry milling the powders (ABB, Wettingen, Switzerland) separately in a tungsten carbide vibrating cup mill (Fritsch Pulverisette 9, Fritsch, Idar-Oberstein, Germany) for 3 min each. The particle size ($D_{V0.5}$) after milling was determined in iso-propanol by means of laser light scattering (Mastersizer S, Malvern Instruments GmbH, Herrenberg, Germany). The data are shown in Table 2.

The milled powders were mixed using appropriate amounts of ZnO, Bi_2O_3 and Sb_2O_3 and distilled water. The total amount of Sb_2O_3 + Bi_2O_3 additives was 1.5 mol% and the pH value of the slurry was 7.5. Mixing was done in a planetary ball mixer for 24 h. A zirconia container and zirconia balls were used to avoid any impurity from the lining. The mixture was dried for 12 h at 130 °C and pushed through a sieve with 2 mm × 2 mm mesh size. The fragments were filled into silicon moulds and cold isostatically pressed at 100 MPa. Cylindrical samples were prepared by machining the pressed compacts. They had a green density of 3.4 g/cm^3—corresponding to a fractional density of 60%.

2.2. Optical dilatometry

For optical dilatometry cylindrical green samples of 20 mm height and 19 mm diameter were used. The samples were sintered in an alumina crucible (inner volume: 42 mm × 30 mm × 25 mm) with closed lid to increase the partial pressure of gas species, evolved during the heat treatment. It had been shown in previous sintering experiments on ZBS green samples without using a closed crucible that evaporation of volatile species (Sb_2O_3, Bi_2O_3) led to insufficient results. The crucible was equipped with sapphire windows at two opposing sides to enable light transmission. It was heated in a chamber furnace by $MoSi_2$ heating elements in air (flow rate 10 l/min). Temperature during sintering was measured with a Pt–PtRh thermocouple outside the crucible. Temperature differences between crucible and furnace were corrected by using an additional thermocouple inside the crucible in separate runs with different heating rates.

For kinetic field studies, samples were heated at different constant heating rates of 1, 2, 5 and 10 K/min up to 1040, 1060,

Table 2
Mean particle size ($D_{V0.5}$) of raw powders and powders after milling in μm.

	ZnO	Sb_2O_3	Bi_2O_3
Raw powder	1.8	3.3	4.4
Milled powder	1.6	2.5	3.3

1080 and 1100 °C, respectively. After holding the samples at these temperatures for 2 h, they were quickly cooled down (at 20 K/min) to room temperature.

The thermooptical measuring principle (TOM) was used for an optical measurement of sample dimensions during sintering [20,21]. The non-contact measurement was considered superior compared to customary push-rod dilatometry because no compressive stress was exerted on the ZnO samples, which are assumed to become rather weak during liquid phase sintering. Shrinkage $L/L_0(T)$ was obtained from the width of the silhouette of the cylindrical samples by scaling with the initial width at the beginning of the measurement. Correction for thermal expansion was done by a 2nd order polynomial fitted to the expansion curve obtained from a sintered ZBS-sample in the required temperature range. Onset temperature of sintering was determined from the $L/L_0(T)$ diagram by the intersection of the horizontal line before shrinkage and the tangent at 1% shrinkage. The temperature to reach 50% of total shrinkage (T_{50}) was derived from the experimental shrinkage curves. Strain rates were calculated by time derivation of the shrinkage curves:

$$\dot{\varepsilon} = \frac{dL}{L\,dt}, \tag{2}$$

where ε = true strain and the dot indicates time derivation.

2.3. Wetting experiments

Wetting of ZnO by the melt phase was investigated by the sessile droplet method, using the thermooptical measuring device already described with the optical dilatometry. A binary (90 vol% Bi_2O_3 + 10 vol% ZnO) and a ternary mixture (90 vol% Bi_2O_3 + 5 vol% ZnO + 5 vol% Sb_2O_3) were heated in an alumina crucible to 740 and 815 °C, respectively. Then the crucible was rotated to cast the melt on to a flat ZnO sample, where it formed a droplet. The contact angle was determined by fitting an ellipse to the droplet contour and by measuring the angle between the horizontal contour line of the ZnO sample and the tangents to the ellipse at the intersection with the horizontal line.

2.4. Quenching experiments

Quenching of the ZnO–Bi_2O_3–Sb_2O_3 (ZBS) samples was done after heating them in air using a small horizontal tube-furnace equipped with positive-temperature-coefficient (PTC) heating elements based on barium titanate. Disk shaped samples with 2 mm thickness and 10 mm diameter were heated with a heating rate of 10 K/min to 800, 900, 1000 and 1100 °C and then rapidly quenched using a liquid nitrogen bath. Quenched samples were then fractured along the flat surface and polished in successive runs using SiC (25 and 15 μm), diamond (3 μm) and finally CeO (1 μm). Polished samples were investigated by scanning electron microscopy (SEM) with backscattered electrons (SUPRA, Carl Zeiss AG, Oberkochen, Germany). The microstructure was analysed by lineal intercept methods by means of Image-C software (IMTRONIC GmbH, Berlin, Germany).

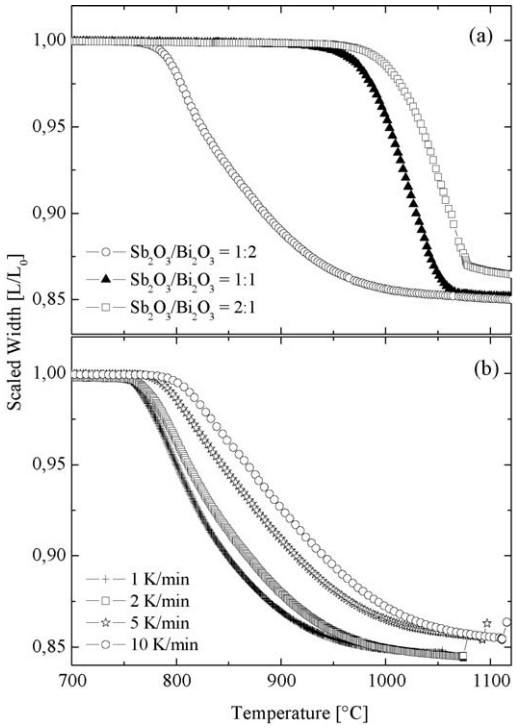

Fig. 1. Shrinkage of ZBS green samples (a) at a heating rate of 5 K/min with different Sb_2O_3/Bi_2O_3 ratios and (b) at different heating rates and a constant Sb_2O_3/Bi_2O_3 ratio of 1:2.

3. Results

3.1. Optical dilatometry

Fig. 1a shows shrinkage curves of ZBS green samples where the molar ratio of Sb_2O_3 to Bi_2O_3 was varied whereas the total concentration of additive materials was kept at 1.5 mol%. The onset of shrinkage decreased drastically from 970 °C, to 944 °C and 790 °C when the Sb_2O_3 to Bi_2O_3 ratio was decreased from 2:1 to 1:1 and 1:2. Note that these samples were prepared from dry mixed unmilled powders.

Fig. 1b shows shrinkage curves for ZBS green samples which were prepared from wet milled powders with a constant molar ratio of Sb_2O_3 to Bi_2O_3 of 1:2 sintered at different heating rates between 1 and 10 K/min. With increasing heating rate, the onset of shrinkage increases from 757 °C to 796 °C. The onset at 5 K/min is 780 °C for the wet milled powder which corresponds to 790 °C for the dry mixed powder. The T_{50} temperatures for the wet mixed and dry mixed powders at a heating rate of 5 K/min are 875 and 850 °C, respectively. This small change of onset and T_{50} temperatures indicates that sintering kinetics was essentially not affected by the preparation process. After the onset of sintering thermal diffusivity usually increases in ceramic green samples [22], i.e. temperature gradients are expected to decrease at constant heating rate. Therefore, the increasing differences between T_{50} temperatures and onset temperatures with increasing heating rate (compare Table 3) were attributed to sintering kinetics and not to temperature gradients.

Table 3
T_{onset} and T_{50} values for milled and wet mixed samples.

	1 K/min	2 K/min	5 K/min	10 K/min
T_{onset} (°C)	757	761	780	796
T_{50} (°C)	823	840	875	899

From the shrinkage data shown in Fig. 1b kinetic field diagrams were constructed. For that, the logarithm of the strain rate was plotted versus inverse absolute temperature. Points representing equal strain on the different strain rate curves were connected to form the so-called iso-strain lines. Details of the method were described by Palmour [23]. It can be seen that the iso-strain lines form straight lines. Due to the Arrhenius type diagram used, the slope of these lines can be interpreted as apparent activation energy for densification (Fig. 3). Since different mechanisms interact during densification, the apparent activation energy does not correspond to one specific mechanism [21].

To investigate the interaction of grain growth and densification in more detail Eqs. (1) and (2) were transformed to use it in the kinetic field diagram. Time derivation, substitution of t and rearrangement leads to:

$$\ln(-\delta T\dot{\varepsilon}) = \ln\left(\frac{C'D_l\gamma_l}{G^n}\right) = \ln\left(\frac{C'D_0\gamma_l}{G^n}\right) - \frac{E_D}{RT}; \qquad \delta = \frac{\Delta L^2 L}{L_0^3} \tag{3}$$

with C' = constant depending on density (different from constant C in Eq. (1)). By plotting the left hand side of Eq. (3) versus inverse absolute temperature liquid phase sintering kinetics can be directly compared to the models for contact flattening and Ostwald ripening, respectively (Fig. 2b).

Fig. 3 shows that the apparent activation energy derived from the slope of the iso-strain lines did not change much with the transformation of the y-axis in the kinetic field diagram. But it is evident from Fig. 2b that the iso-strain lines related to strain values between 0.96 and 0.91 are parallel and close to one single line. This suggests that – in this strain range – sintering kinetics is controlled completely by the right term: $E_D/(RT)$ in Eq. (3) whereas the logarithm: $\ln(C'D_l\,\gamma_{lv}G^{-n})$ is constant.

Eq. (3) was fitted to the experimental iso-strain lines of Fig. 2b using an in-house least square fitting software which was based on a gradient search algorithm. For that, the measured ZnO particle size of 1.56 μm was used as G_0 (see Table 2). Different exponents for grain growth m and densification n between 3 and 6 were tested in the fits. The smallest χ^2 was obtained with $n = 3$, $m = 3$, respectively with $n = 4$, $m = 4$. In this range of exponents the quality of the fits was good and small differences in χ^2 were considered not significant. The fitted parameters are shown in Table 4. The range indicates the variation of the respective parameters within the acceptable range of exponents. A kinetic field diagram obtained from the theoretical strain rate curves is shown in Fig. 4. Good agreement to the experimental iso-strain lines was obtained.

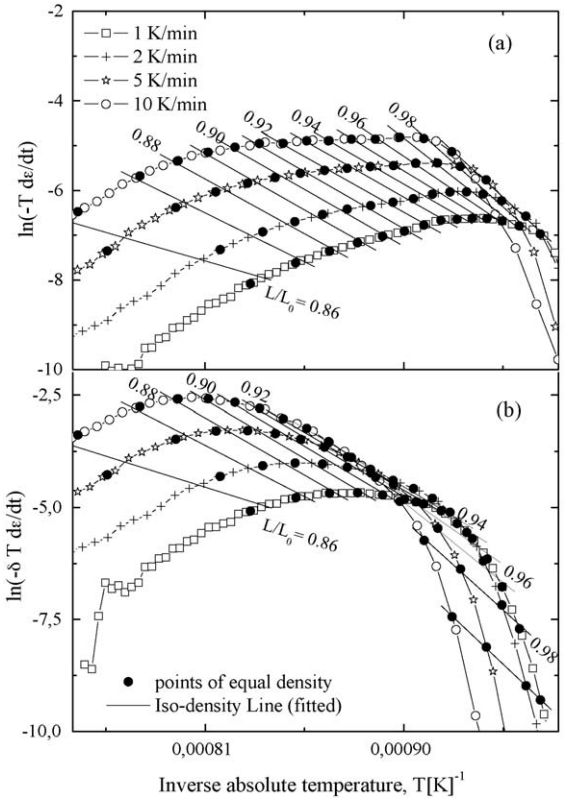

Fig. 2. Kinetic field diagram of the data shown in Fig. 1b with iso-strain lines: (a) plotted in the standard way, (b) plotted after transformation of y-axis according to Eq. (3).

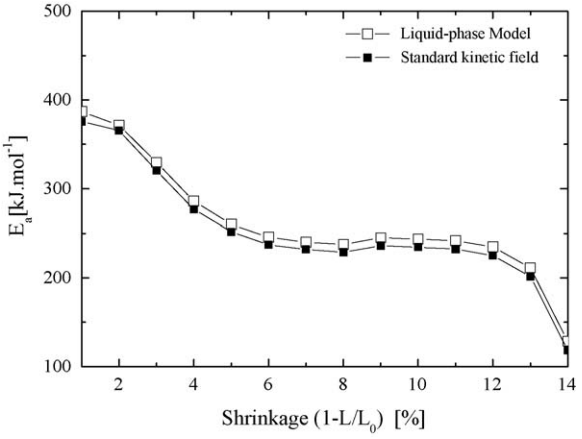

Fig. 3. Apparent activation energy (E_a) as a function of linear shrinkage for ZBS sample using standard and liquid-phase kinetic field (compare Fig. 2).

Table 4
Fitted grain sizes of ZnO G_{ZnO} and activation energies for diffusion E_D respectively grain growth E_G during sintering of ZBS green samples at a heating rate of 10 K/min.

Temperature (°C)	G_{ZnO} (μm)	E_D (kJ/mol)	E_G (kJ/mol)
800	1.56	500 ± 20	570 ± 10
900	2.1–2.7		
1000	6.2–7.3		
1100	13.2–17.6		

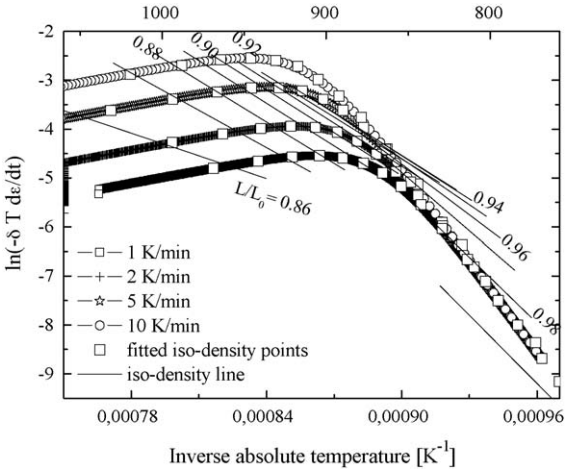

Fig. 4. Kinetic field diagram re-produced by fitting experimental iso-density lines to Eq. (3) ($n = 3$ and $m = 4$).

3.2. Microstructure analysis

To complement the findings from the kinetic field analysis, the microstructures of partially sintered and quenched ZBS samples were investigated. Fig. 5 shows SEM images of polished sections of green samples heated to different temperatures with a heating rate of 10 K/min. ZnO can be distinguished by its grey contrast from the darker pores and a brighter inter-grain phase. The different constituents of the inter-grain phase (Bismuth oxide, pyrochlore, and spinel) were not distinguished. The average chord lengths of ZnO grains, pores and inter-grain phase were obtained from lineal intercept analysis of the SEM images (Fig. 6a). A steep increase of ZnO grain size was measured between temperatures of 900 and 1000 °C. The growth of ZnO grains was accompanied by a coarsening of pores and inter-grain phase, where the inter-grain phase showed smaller chord lengths compared to the pores at the respective temperature (compare Fig. 6a).

The chord lengths of ZnO grains followed a log-normal distribution and hence average grain sizes were calculated using Mendelsons model [24],

$$G = K_M L_c \tag{4}$$

where G is average grain size in 3D, K_M is Mendelsons conversion constant and L_C is the average chord-length. The

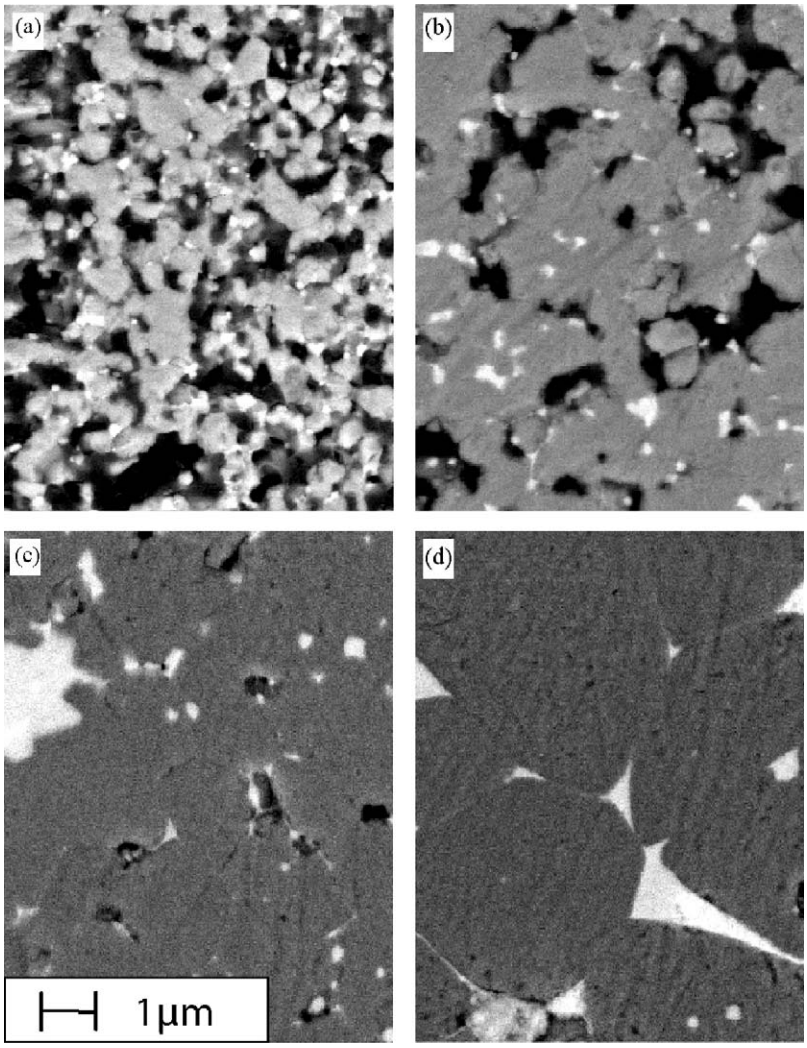

Fig. 5. Backscattered electron micrographs of ZBS samples quenched into liquid nitrogen from (a) 800 °C, (b) 900 °C, (c) 1000 °C and (d) 1100 °C.

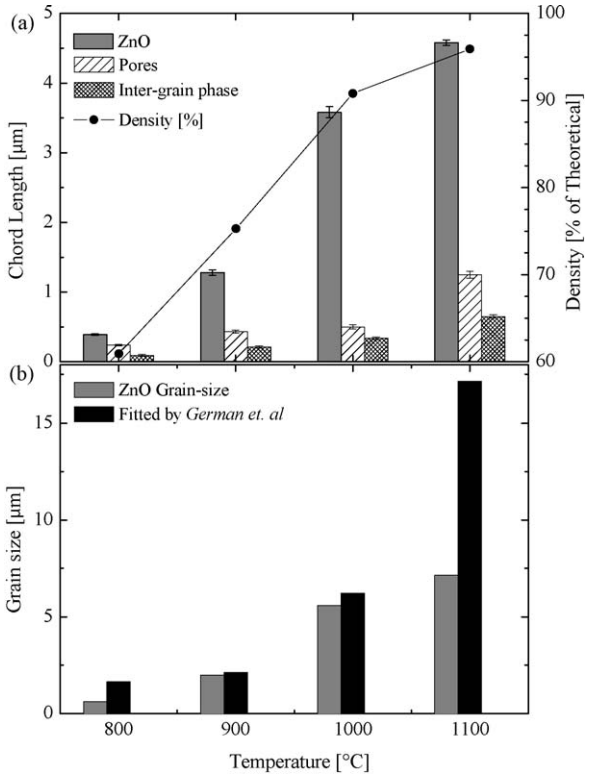

Fig. 6. (a) Chord-lengths of ZnO- grain, inter-grain phase and pores and (b) average grain sizes of ZnO from chord-length (grey) and from fitting Eq. (3) (black) as function of quenching temperature. Corresponding density values obtained from in situ dilatometer are also shown on the right y axis of (a).

value of K_M was chosen to be 1.56 according to Senda and Bradt [14].

Fig. 6b compares the ZnO grain sizes from the microstructure analysis with the grain size obtained from fitting Eq. (3) to the kinetic field data (compare Table 4). A good agreement between both methods was obtained. Note that the larger difference in the final sintering stage can be attributed to the scope of Eq. (3) which covers the intermediate sintering stage only.

3.3. Wetting behaviour of the melt phase

Using the ternary mixture which includes Sb_2O_3, the melting was shifted to higher temperatures above 800 °C compared to the binary mixture where it occurred close to the eutectic temperature of 738 °C. Therefore, the wetting experiments were performed at two different temperatures. Fig. 7 shows the contact angle after depositing a droplet of the binary or ternary mixture on the ZnO substrate. The contact angles were very small. They decreased slightly and approached 5° for the binary powder mixture and 1° for the ternary powder mixture after about 20 min.

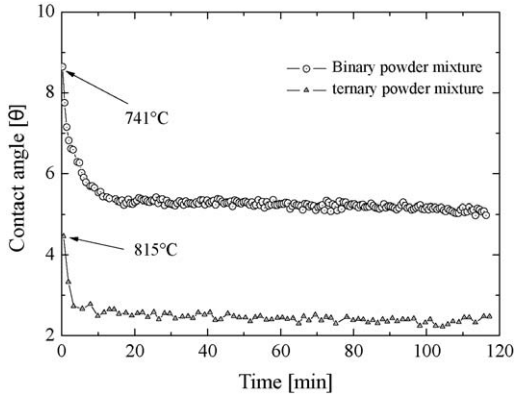

Fig. 7. Wetting of pure ZnO substrate by binary (○) and ternary (Δ) powder mixtures. Note that the melting points are different.

4. Discussion

The large impact of the molar ratio of Sb_2O_3 and Bi_2O_3 on sintering kinetics shown in Fig. 1a confirms various measurements by other groups (compare, e.g. [11]). It was explained by the formation of solid pyrochlore ($Zn_2Bi_3Sb_3O_{14}$) which requires an equimolar ratio of both sesquioxides [11]. The 1:2 molar ratio of Sb_2O_3 and Bi_2O_3 allows for an early melt formation from excess Bi_2O_3 which explains the low onset temperature of 760 °C—only slightly above the eutectic temperature of 738 °C in the binary ZnO–Bi_2O_3 system. An increase of the melting temperature to 760 °C was predicted from thermodynamic modelling for the ternary ZnO–Bi_2O_3–Sb_2O_4 system [25]. This increase was experimentally verified in the present study by the wetting experiments using binary and ternary mixtures of Bi_2O_3 and ZnO and Bi_2O_3, ZnO and Sb_2O_3 respectively. The increase of onset temperature with increasing heating rate (compare Fig. 1b) was attributed to heat flow within the samples and initial local sintering after melt formation. Pyrochlore decomposes at a temperature around 1000 °C and spinel ($Zn_7Sb_2O_{12}$) is formed [11]. Thereby Bi_2O_3 is released and sintering can proceed—also in the systems with molar ratios of Sb_2O_3 and $Bi_2O_3 \leq 1$ (compare Fig. 1a).

The apparent activation energy for the sintering of ZBS green samples, which was derived from the slope of the iso-strain lines, is in the range of 200–400 kJ/mol—decreasing during densification (compare Fig. 4). It is much smaller than the activation energy for diffusion of ZnO species in the melt phase of 500 kJ/mol, which was derived from the fit of Eq. (3) (compare Table 4). The difference is explained by the counteraction of grain growth and diffusion with respect to densification. Both phenomena are thermally activated. They show a strong increase in temperature, but the diffusion coefficient appears in the numerator, whereas the grain size controls the denominator (compare Eq. (3)). The activation energy of 580 kJ/mol for grain growth is higher than the activation energy for diffusion. Therefore, the counteraction leds to an anticlockwise rotation of iso-strain lines with increasing density. This can be understood if two points A and B on an iso-strain line in intermediate sintering stage are examined (compare Fig. 8). Point A is obtained from a sintering experiment with a low heating rate and point B from a sintering run with high heating rate. The temperature increase, which is required for a strain decrement $\Delta L/L_0$ to reach points A′ and B′ at the next iso-strain line, depends on grain growth. At the smaller heating rate grain growth rate is relatively smaller compared to diffusion rate because the temperatures are smaller than at the higher heating rate and the activation energy for

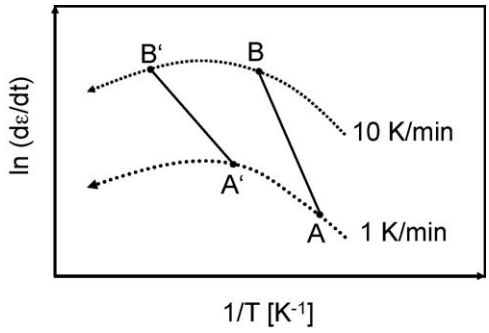

Fig. 8. Schematic diagram showing rotation of iso-strain line AB when going to next line A′B′ in a kinetic field diagram ($E_G > E_D$ see text).

grain growth was higher than the activation energy for diffusion. This means the distance A–A′ is smaller than the distance B–B′, which explains the anticlockwise rotation (compare Fig. 8). It is to be noticed that a parallel shift of iso-strain lines is expected if $E_D = E_G$ and a clockwise rotation if $E_D > E_G$ [26].

The activation energy for grain growth of 580 kJ/mol is rather high compared to the activation energies presented by other groups (see Table 1). It is assumed that this activation energy also reflects a mixture of different mechanisms. So the Zener drag process for spinel particles or pores at the ZnO grain boundary interferes with the growth process from Ostwald ripening. Presumably the Zener drag process and Ostwald ripening have different activation energies. The counterplay of the two mechanisms may lead to similar decrease of apparent activation energy for grain growth as it was described for densification in the previous paragraph.

The modified kinetic field diagram shown in Fig. 2b is considered superior to the standard representation (compare Fig. 2a) in describing liquid phase sintering. The transformation of the y-axis according to liquid phase sintering models allows for a direct identification of grain growth. Grain growth leads to a shift of iso-strain lines to the left hand side in the kinetic field diagram, because it increases the denominator in Eq. (3). This has to be compensated by an increased diffusion coefficient in the numerator which requires higher temperatures. From the modified kinetic field the onset of considerable grain growth can be directly recognised by the shift of iso-strain lines. In the present example this shift occurs at a strain of 0.9 (compare Fig. 2b). At a heating rate of 10 K/min this strain corresponds to a temperature of 950 °C (compare Fig. 1b). It is in the temperature range of fast grain growth which was identified by microstructure analysis (compare Fig. 6).

The magnitude of the shift of the iso-strain lines to the left hand side provides a measure for the grain growth rate which can be used to compare sintering behaviour of different green samples. The change of the slope of the iso-strain lines, i.e. anticlockwise rotation of ZBS green samples in the present example, enables direct conclusions on the heating cycle required for a change in the grain size of dense samples. So for the ZBS samples it was concluded from Fig. 2 that a longer holding period at lower temperatures leads to smaller grains at same density than a shorter holding period at higher temperatures. It was reported for customary and nanoparticle ZnO based varistor ceramics that a holding period at lower temperature leads to a finer microstructure indeed [27,28].

In the initial sintering stage the iso-strain lines shift to the right hand side. This can be seen in Fig. 2b for $L/L_0 = 0.98$, 0.96 and 0.94. Eq. (3) cannot be applied in this stage because it is based on models for intermediate stage sintering. Apart from this shift of iso-strain lines an intersection of strain rate curves in the low temperature regime is observed for both types of kinetic field diagrams (compare Fig. 2a and b). Initially, strain rates at lower heating rates are higher than at higher heating rates. In the intermediate sintering stage the usual relation between strain rates and heating rates is restored. A similar transposition in the initial sintering stage was not observed for solid state sintering processes (compare, e.g. [26]). It was assumed that a slow mechanism, which is not affected much by temperature, retards densification in this stage. Such a mechanism could be the redistribution of liquid phase. The redistribution is controlled by wetting properties, and viscosity of the melt and pore size distribution of the compact. The contact angle experiments for the ZBS system had shown that the melt has good wetting behaviour. The viscosity of the melt is assumed to be small, which would allow a fast redistribution.

From the microstructure investigation of a large number of quenched specimen it was always observed that the melt fills part of the pores completely whereas other pores are filled completely by the vapour phase (compare Fig. 5). This separation of the two fluid phases is in contrast to theoretical liquid phase distributions reported in literature where the liquid is arranged around the particle contacts in the initial sintering stage [29]. It was assumed that the driving force for the separation is the liquid–vapour interfacial energy. The liquid–vapour interface can be drastically reduced by the separation of both fluid phases.

The average chord length for the inter-grain phase was smaller than the average chord length of the pores (compare Fig. 6a). This could be interpreted as a confirmation of the pore filling theory which claims a preferred filling of smaller pores by wetting melts during liquid phase sintering [30]. A thermodynamic justification was given for the pore filling theory, which considers the larger specific surface of smaller pores and correspondingly larger decrease of interface energy, when filled by the melt compared to larger pores. However, in the present study a closer look to the microstructures showed that during the entire sintering cycle also large pores were filled by the liquid phase. This was explained by an energy barrier which prevents redistribution according to the thermodynamic minimum (Fig. 9). The redistribution requires an intermediate state where pores are only partially filled. The additional liquid–vapour interface within these pores costs additional energy. So an activation energy exists which hinders liquid redistribution according to the thermodynamic minimum.

Considering this energy barrier, an initially inhomogeneous distribution of the melt phase leads to local shrinkage in the regions surrounding pores which are filled by the melt whereas no shrinkage occurs in other regions. After some shrinkage the local decrease of pore volume causes squeezing out of liquid

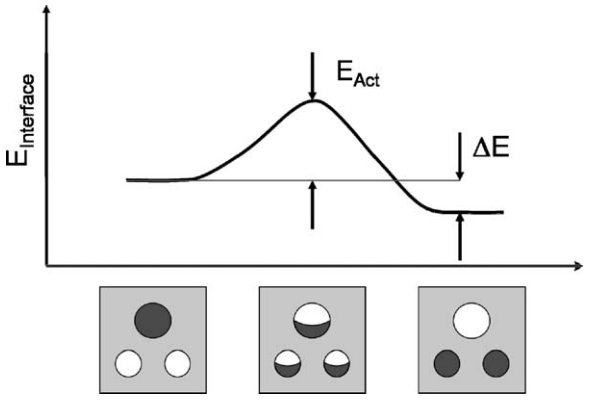

Fig. 9. Interface energy during liquid redistribution—starting from a filled large pore and two empty smaller pores (left), versus partially filled pores (middle), and ending with an empty large pore and two filled smaller pores (right).

towards neighbouring regions which can subsequently sinter. Although this leads finally to high densification in all regions, a delay of shrinkage in the initial sintering stage is expected. This delay is in agreement to the transposition of iso-strain lines to higher rates with increasing strains observed in the initial sintering stage (compare Fig. 2b). Inhomogeneous microstructures of the sintered ceramics can origin from this kinetic effect. Grain growth, for example, is faster in regions which are already dense because the grain boundary mobility is not decreased by pores. In the ZBS system – at temperatures below 1000 °C – an additional increase of local grain growth can be caused by the absence of spinel particles.

5. Conclusions

It was shown that a modified kinetic field technique can be used to adequately describe liquid phase sintering. It was based on general liquid phase sintering models for Ostwald ripening and contact flattening. From the kinetic field diagram conclusions were obtained on microstructural changes during sintering. This information is considered important for an efficient process optimisation of liquid phase sintering. Both, the fit of kinetic equations to the kinetic field data and the microstructure analysis were done in the present work to demonstrate that a reasonable agreement between the methods is achieved. But it is emphasised that neither fitting nor microstructure analysis are required to obtain conclusions on the heating cycle or to compare sintering activity of different green samples. This is considered the most important result for practical applications because it enables an efficient optimisation of the manufacturing process by means of basically four sintering runs per type of green sample and the construction of the respective kinetic field diagram. A shift of the iso-strain lines in the initial sintering stage towards higher strain rates with increasing strain indicates mechanisms which retard sintering and which show small temperature dependence. A shift towards lower rates indicates thermally activated coarsening of the microstructure. A rotation of the iso-strain lines indicates different activation energies for coarsening and densification. Anticlockwise rotation – with increasing strain – shows that the activation energy for grain growth is larger than for densification and a smaller sintering temperature is advantageous for a small final grain size and vice versa.

It was shown that an energy barrier can prevent redistribution of the melt phase according to thermodynamic minimum. This requires a careful homogeneous distribution of Bi_2O_3 in the green body to achieve a homogeneous microstructure of the sintered varistors.

Acknowledgements

The authors are grateful to Gerd Mueller of Fraunhofer ISC, Josef Breu of University of Bayreuth, Germany and Mr. Felix Greuter of ABB, Switzerland for their valuable advices and suggestions and also to the *Elitenetzwerk*, *Bayern* for their financial support to carry out the research work.

References

[1] M. Matsoka, Nonohmic properties of zinc oxide ceramics, Jpn. J. Appl. Phys. 10 (1971) 736–746.
[2] R.C. Bradt, S.L. Burkett. Microstructural control of zinc oxide varistor ceramics. In: Tomsia, A.P., Glaeser, A.M. (Eds.), Ceramic Microstructures—Control at the Atomic Level. (1998) pp. 339–348.
[3] D.R. Clarke, Varistor ceramics, J. Am. Ceram. Soc. 82 (3) (1999) 485–502.
[4] L.M. Levinson, H.R. Philipp, Zinc oxide varistors—a review, Am. Ceram. Soc. Bull. 65 (4) (1986) 639.
[5] W.G. Morris, Physical properties of the electrical barriers in varistors, J. Vac. Sci. Technol. 13 (1976) 926–931.
[6] E. Olsson, G.L. Dunlop, Characterization of individual interfacial barriers in a ZnO varistor material, J. Appl. Phys. 66 (1989) 3666–3675.
[7] M. Bartkoviak, G.D. Mahan, Phys. Rev. B: Condens. Matter 51 (1995) 1025–1032.
[8] M. Inada, Crystal phases of nonohmic zinc oxide ceramics, Jpn. J. Appl. Phys. 17 (1) (1978) 1–10.
[9] K.G. Vasantha Kumari, P. Divya Vasu, V. Kumar, T. Asokan, P.K. Davies, Formation of zinc–antimony-based spinel phases, J. Am. Ceram. Soc. 85 (2001) 703–705.
[10] J.P. Guha, S. Kunej, D. Suvorov, Phase equilibrium relations in the binary system Bi_2O_3–ZnO, J. Mater. Sci. 39 (2004) 911–918.
[11] K. Jinho, K. Toshio, Y. Takashi, Sintering of zinc oxide doped with antimony oxide and bismuth oxide, J. Am. Ceram. Soc. 72 (8) (1989) 1390–1395.
[12] S. Takajo, W.A. Kaysser, G. Petzow, Analysis of particle growth by coalescence during liquid phase sintering, Acta Met. 32 (1984) 107–113.
[13] W.D. Kingery, Densification during sintering in the presence of a liquid phase. I. Theory, J. Appl. Phys. 30 (1959) 301–306.
[14] T. Senda, R.C. Bradt, Grain growth in ZnO and ZnO–Bi_2O_3 ceramics, J. Am. Ceram. Soc. 73 (1) (1990) 106.
[15] D. Dey, R.C. Bradt, Grain growth of ZnO during liquid phase sintering, J. Am. Ceram. Soc. 75 (9) (1992) 2529–2534.
[16] T. Senda, R.C. Bradt, Grain growth of zinc oxide during the sintering of zinc oxide–antimony oxide ceramics, J. Am. Ceram. Soc. 74 (6) (1991) 1296.
[17] S.I. Nunes, Grain growth of ZnO in ZnO–Bi_2O_3 ceramics with Al_2O_3 additions, J. Am. Ceram. Soc. 18 (9) (1995) 2469–2475.
[18] H. Suzuki, R.C. Bradt, Grain growth in ZnO in ZnO–Bi_2O_3 ceramics with TiO_2 additions, J. Am. Ceram. Soc. 78 (5) (1995) 1354–1360.
[19] Y.-C. Chen, C.-Y. Shen, L. Wu, Grain growth processes in ZnO varistors with various valence states of manganese and cobalt, J. Appl. Phys. 69 (12) (1991).
[20] F. Raether, R. Springer, St. Beyer, Optical dilatometry for the control of microstructure development during sintering, Mater. Res. Innovations 4 (2001) 245–250.

[21] F. Raether, Current state of in-situ measuring methods for the control of firing processes, J. Am. Ceram. Soc. 92 (2009) 146–152.
[22] F. Raether, R. Springer, In-situ measurement of neck formation during sintering of alumina by a novel thermooptical measuring device, Adv. Eng. Mater. 2 (2000) 741–744.
[23] H. Palmour III, Rate-controlled sintering technology for PM and composites, Powder Met. Report 9 (1988) 572.
[24] M.I. Mendelson, Average grain size in polycrystalline ceramics, J. Am. Ceram. Soc. 52 (8) (1969).
[25] M.L. Arefin, F. Raether, D. Doleijš, A. Klimera, Experimental study of phase formation during liquid phase sintering of ZnO ceramics, Ceram. Int. 35 (2009) 3313–3320.
[26] F. Raether, P. Schulze Horn, Investigation of sintering mechanism of alumina using kinetic field and master sintering diagrams, J. Eur. Ceram. Soc. 29 (2009) 2225–2234.
[27] B. Balzer, M. Hagemeister, P. Kocher, L.J. Gauckler, Mechanical strength and microstructure of zinc oxide varistor ceramics, J. Am. Ceram. Soc. 87 (2004) 1932–1938.
[28] P. Duran, J. Tartaj, C. Moure, Fully dense, fine-grained, doped zinc oxide varistors with improved nonlinear properties by thermal processing optimization, J. Am. Ceram. Soc. 86 (2003) 1326–1329.
[29] R.M. German, Sintering Theory and Practice, Wiley, New York, 1996.
[30] Y.P. Kim, S.W. Jung, S.J.L. Kang, Enhanced densification of liquid-phase-sintered WC–Co by use of coarse WC powder—experimental support for the pore-filling theory, J. Am. Ceram. Soc. 88 (2005) 2106–2109.